Journal of Materials Chemistry B

Materials for biology and medicine

rsc.li/materials-b

ROYAL SOCIETY
OF CHEMISTRY
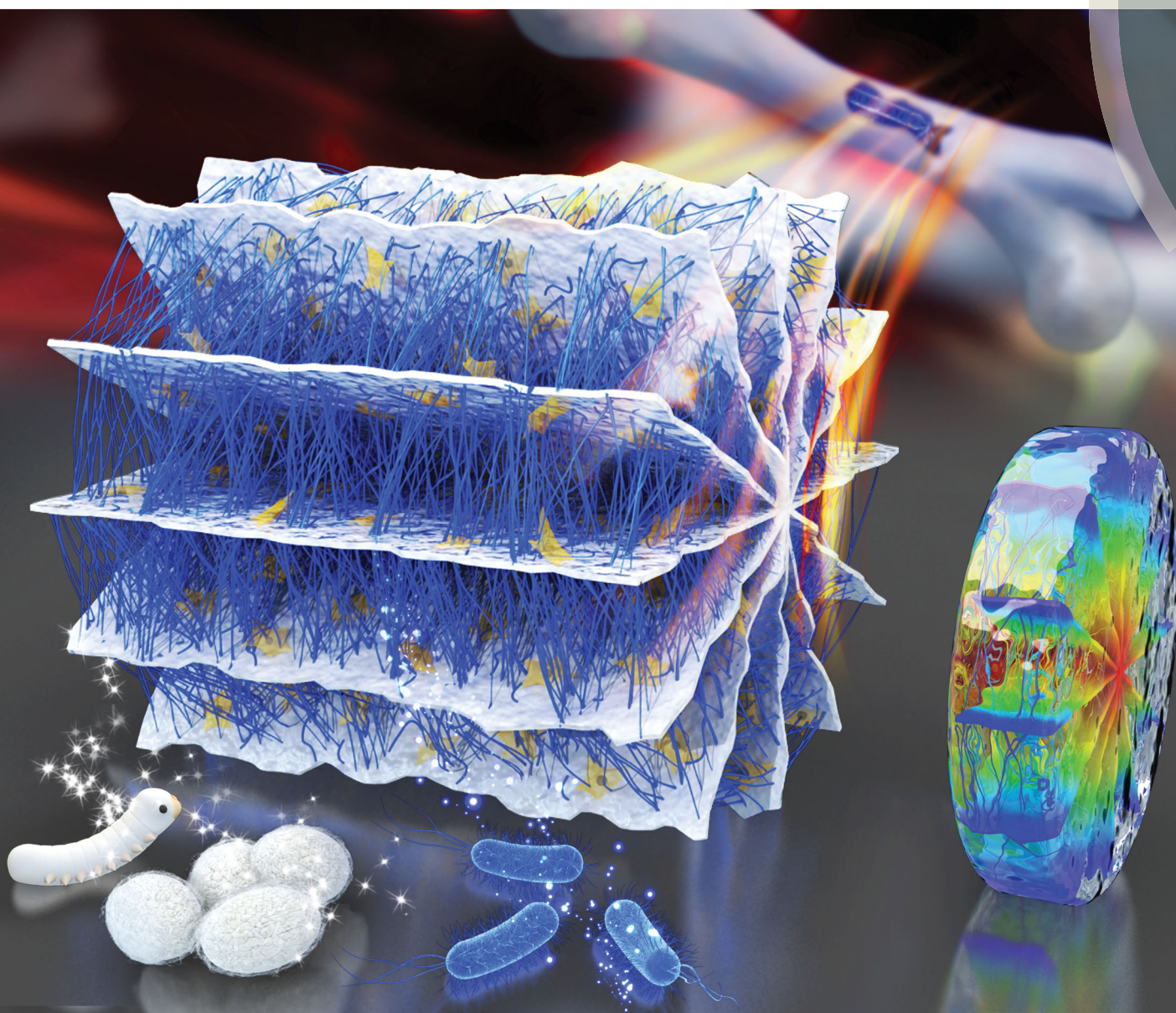
PAPER
Yaopeng Zhang *et al.*
Robust silk fibroin/bacterial cellulose nanoribbon composite scaffolds with
radial lamellae and intercalation structure for bone regeneration

PAPER

Check for updates

Robust silk fibroin/bacterial cellulose nanoribbon composite scaffolds with radial lamellae and intercalation structure for bone regeneration†

Jian Chen,‡ Ao Zhuang,‡ Huili Shao, Xuechao Hu and Yaopeng Zhang ⓘ *

A big challenge in bone regeneration is preparation of an appropriate bone extracellular matrix that mimics the robust mechanical properties of the lamellar structure of natural bones as well as the *in vivo* micro-environment of bone cells. In this work, silk fibroin (SF)/bacterial cellulose nanoribbon (BCNR) composite scaffolds were prepared using various BCNR contents *via* a multi-staged freeze-drying method. The scaffolds showed a radial lamellar pattern and gradient lamellae gap distance, the structure of which could transfer nutrient solution and metabolic waste through a capillary effect, and can guide cells from the outer to the inner area of the scaffolds. The gap distance and thickness of the lamellae increased with increasing BCNRs contents. Parts of BCNRs attached to the surfaces of lamellae while others penetrated into it. The intercalation structure led to an eight-fold enhancement in compression modulus and six-fold increase in compression strength. These robust three-dimensional composite scaffolds with improved *in vitro* bioactivity, bone-cell adhesion, and proliferation are highly promising for further applications in bone defect repairs.

Introduction

Bone defects, especially those of large size caused by diseases or injury, are difficult to heal naturally.[1] Nowadays, the best possible clinical therapy for this is an autologous bone graft, the "gold standard" for treatment of critical-sized defects. However, the rarity of sources for autologous bone grafts and infection of donor sites restrict further application.[2,3] To tackle this problem, tissue engineering has been applied to fabricate three-dimensional scaffolds, thereby providing frames or substrates that allow cells to attach and proliferate.[4–6] "Ideal" tissue scaffolds should have at least four requirements: (1) good biocompatibility, (2) an appropriate rate of biodegradability that matches the tissue growing rate, (3) an interconnected porous structure that allows flow of nutrients or waste so that cell viability is maintained, and (4) considerable mechanical strength that can sustain the attachment and proliferation of cells.[7] Until now, utilization of polymeric biomaterials has been limited because of their failure to address compressive strength

in load-bearing bone grafts.[8] Also, they posses a large pore-sized structure, which generally leads to poor mechanical properties. In addition, single-component scaffolds are usually weak, composite types composed of multiple materials. Hence, they have become more promising for building suitable bone replacements that have a "tunable" mechanical property and pore structure.[9,10]

In most functional tissues, such as nerves, tendons, and vessels, the various scaffolds need to have aligned and anisotropic morphology because they present obvious anisotropic behavior.[11–14] Moreover, the mechanical properties of scaffolds have considerable influence on inoculated cells. High stiffness not only boosts the adherence and migration of cells,[15,16] but also promotes the differentiation of stem cells to become bone cells or tissues.[17] Therefore, this work aimed to build strengthened composite scaffolds that possess aligned lamellae.

Silk fibroin (SF) derived from silkworm is a good candidate for tissue engineering scaffolds owing to its excellent biocompatibility, tunable biodegradability, rare inflammatory response, antibiotic property, and good permeability (to water vapor and oxygen).[18,19] considerable research has been conducted to fabricate SF scaffolds *via* particle leaching,[20] compression molding,[21] three-dimensional (3D) printing,[22] gas foaming,[23,24] lyophilization,[25–27] and electrospinning.[28–31]

Bacterial cellulose produced from *Acetobacter xylinum* possesses a natural 3D nano-network structure, high purity, high Young's modulus and strength, as well as good biocompatibility. Hence, cell adhesion is promoted, and many hydroxyl groups can

State Key Laboratory for Modification of Chemical Fibers and Polymer Materials, College of Materials Science and Engineering, Donghua University, Shanghai 201620, China. E-mail: zyp@dhu.edu.cn; Fax: +86-21-67792855; Tel: +86-21-67792954

‡ J. Chen and A. Zhuang contribute equally to this work.

promptly interact with other polymers.[32–38] Therefore, bacterial cellulose is another good candidate for bone tissue engineering scaffolds, although its nanopore structure limits further applications. In the present study, bacterial cellulose nanoribbons (BCNRs) were applied to build an intercalation structure and to reinforce SF scaffolds. Furthermore, the influence of BCNRs content on the morphology, and mechanical and biological properties of the composite scaffolds was investigated.

Experimental

Preparation of BCNRs and SF aqueous solutions

BCNRs were prepared using bacterial cellulose bulk supplied by Hai Nan Yeguo Foods (China). Bacterial cellulose bulks were boiled twice in 0.5% (w/v) sodium carbonate aqueous solution to remove *Acetobacter xylinum* and then washed with deionized water. After soaking for 3 days until the pH of the filtrate was neutral, the purified bacterial cellulose bulks were chopped by a homogenizer (T18DS25; IKA, Germany) at 10 000 rpm for 15 min. The solid BCNRs were dehydrated by lyophilization for 12 h. SF solution was prepared according to a procedure described previously.[39] Briefly, cocoons of *Bombyx mori* were boiled twice for 30 min in an aqueous solution of 0.5% (w/v) sodium carbonate and then rinsed with deionized water to remove sericin and residual sodium carbonate. After that, the degummed silk fiber was dissolved in 9.0 M aqueous lithium bromide solution at 40 °C for 2 h. The solution was subsequently centrifuged and filtered to remove impurities before being dialyzed in a semi-permeable cellulose membrane (molecular weight cut-off (MWCO) = 14 kDa) for 3 days. The SF solution was concentrated further to 12% (w/v) using forced airflow at 4 °C.

Preparation of neat SF and composite scaffolds

SF aqueous solution (12% (w/v)) and BCNR solid powder were poured into stainless-steel molds with BCNR/SF weight ratios of 0 : 20, 1 : 20, 2 : 20, 3 : 20, and 4 : 20. The mixtures were then stirred by a magnetic bar at 1000 rpm for 15 min, and subsequently treated with ultra-sonication for 30 s to promote homogeneity. After precooling at −25 °C for 6 h, the samples were stored at −80 °C overnight. Finally, they were lyophilized to generate lamellar scaffolds, which were then treated with 90% (v/v) ethanol for 6 h to induce water insolubility in the scaffolds.

Transmission electron microscopy (TEM)

The homogenized BCNRs were diluted to 0.01 mg mL^{-1} by deionized water. The diluted solution was then instilled to a copper net to collect the BCNRs. The specimen was observed by TEM using a JEM-2100 (JEOL, Japan) system at 200 kV. Two-hundred counts were conducted at each position to measure the diameter of BCNRs.

Scanning electron microscopy (SEM)

The composite scaffolds were frozen in liquid nitrogen and sliced in cross-section. After being sputtered with platinum, the cross-section of the samples was observed using a scanning electron microscope (JSM-5600LV; JEOL) at 8 kV. To assess the lamellar structure along the radial direction of the scaffolds, images taken from the edge to the center of the cross section were used for further image mosaics. The gap distance and thickness of lamellar were measured through Nano Measurer 1.2 software. One-hundred counts were conducted at each position.

Synchrotron radiation wide-angle X-ray diffraction (SR-WAXD)

SR-WAXD was conducted to characterize the crystalline structure of the scaffolds using BL15U beamline equipped with a Rayonix-165 detector at Shanghai Synchrotron Radiation Facility. The samples were sliced into cuboids, each with dimensions of 10 mm × 10 mm × 1 mm. The calibration was conducted using a ceric oxide standard. The distance from the sample to the detector was 160 mm. The X-ray wavelength was 0.07746 nm and the diameter of the beamstop was 10 mm. The spot size of the X-ray beam was 4 × 2.75 μm^2.

Fourier transform infrared (FTIR) spectroscopy

The composite scaffolds were sliced into laminae and dried in an oven for 2 h prior to being tested by a Nicolet 6700 Fourier transform Infrared spectrometer (Thermo Fisher, USA), which employed attenuated total reflectance. At a resolution of 0.09 cm^{-1}, the experimental wavenumbers ranged from 600 to 4000 cm^{-1}.

Mechanical properties

Mechanical properties of the columnar composite scaffolds (height of 15 mm × diameter of 10 mm; five samples in each group) were determined using a material testing instrument (5565; Instron, USA) equipped with a 10 kN load cell at a compressive rate of 3 mm min^{-1}. The testing temperature and relative humidity were 25 ± 2 °C and 50 ± 5%, respectively. The compressive modulus was determined from the slope of the initial linear part of the curve, and strength was confirmed by interception of a parallel line starting at 1% strain and the curve.[20]

Porosity

The scaffolds were neatly cut into multiple rectangles of the corresponding volumes (unit: cm^3). The porosity (P) of the composite scaffolds was determined using the following equation:

$$P\ (\%) = 1 - \frac{\rho_a}{\rho_r} \qquad (1)$$

where the apparent density (ρ_a) was the ratio of the mass of a dry scaffold (g) and its volume (cm^3), and real density (ρ_r) was measured using Ultrapyconometer100 (Quantachrome, USA) at 25 ± 2 °C.

Evaluation of the swelling ratio and water uptake of composite scaffolds

The composite scaffolds were soaked in deionized water at 25 ± 2 °C for 24 h. Prior to measuring the wet weight of the scaffolds (W_s), excess water was thoroughly removed with filter paper. The dry weight (W_d) of the scaffolds was obtained from samples oven-dried at 60 °C for 24 h. At least three scaffolds were used

for each measurement. The swelling ratio and water uptake were calculated according to the following equations:[40,41]

$$\text{Swelling ratio} = \frac{W_s - W_d}{W_d} \qquad (2)$$

$$\text{Water uptake (\%)} = \frac{W_s - W_d}{W_s} \times 100\% \qquad (3)$$

Evaluation biocompatibility *in vitro* by cell culture

The composite scaffolds were cut into chips of diameters 15 mm and thicknesses of 1 mm, and placed in 24-well plates. The chips were soaked in 75% (v/v) ethanol for 2 h for sterilization and then washed with phosphate-buffered saline (PBS) to remove ethanol. In the MTT assay, bone cells (MC3T3) were seeded at 5×10^4 cells per well and cultured at 37 °C in an atmosphere of 5% CO_2. The control groups were culture plates and glass coverslips. To determine viability, cells were subjected to the MTT assay.[13] The complete MTT assay protocol can be found in ESI.† The cell morphology on the composite scaffolds was observed by SEM and fluorescence microscopy. First, the MC3T3 cells were seeded on composite scaffolds at 2×10^4 cells per well for 1–5 days. Then, paraformaldehyde (4% (v/v)) was added to the wells and incubated for 2 h at 4 °C.[42] The composite scaffolds prepared for SEM were washed thrice with PBS and then dehydrated with various concentrations of ethanol (50, 60, 70, 80, 90, 95, and 100% (v/v)).[12] The scaffolds were sputtered with platinum prior to SEM imaging at 8 kV.

For fluorescence microscopy, the immobilized scaffolds seeded for 1, 2, 3 and 5 days were washed twice with PBS, then soaked with 300 µL of 0.1% (v/v) Triton X-100 for 5 min. After washing with PBS again, the scaffolds were incubated with 300 µL of 1% (w/v) bovine serum albumin for 15 min. Finally, the scaffolds were stained with calcein-labeled phalloidin for 20 min. A fluorescence microscope (BX51; Olympus, Japan) was used for fluorescence imaging. All operations were performed at 25 ± 2 °C.

In vitro bone bioactivity assay

Simulated body fluid (SBF) was prepared according to the formulation designed by Kokubo.[43] The inorganic constituents of SBF are similar to those of human plasma. The composite scaffolds were first immersed in SBF at 37 °C for 5 days, and then gently rinsed with deionized water prior to drying at 37 °C overnight. Finally, the mineralized scaffolds were sputtered with platinum and observed by SEM (JSM-5600LV; JEOL) at 13 kV. The hydroxyapatite area in the cross-sectional SEM images was analyzed using Image Pro Plus v6.0 (Media Cybernetics, USA). The relative content of mineralized hydroxyapatite (mineralization ratio) was calculated as the ratio of hydroxyapatite area to total solid area in SEM images.

Data analyses

Data are average values with standard deviation. Probability values were calculated using one-way ANOVA, and $p < 0.05$ was considered statistically significant.

Results

Morphology of BCNRs

Fig. 1 shows the TEM image and diameter distribution of BCNRs. They demonstrate clear ribbon structures with a relatively narrow distribution of diameters. Most BCNRs had diameters ranging from 30 to 80 nm. Furthermore, the homogenized BCNRs had a bifurcate structure, which is similar to fiber fibrillation. This might be beneficial to reinforce SF scaffolds.

Morphology of composite scaffolds

The neat SF and composite scaffolds with BCNR/SF weight ratios of 0 : 20, 1 : 20, 2 : 20, 3 : 20, and 4 : 20 were assigned as CS0, CS1, CS2, CS3, and CS4, respectively. CS1 cross-sectional SEM images revealed that the scaffolds had radial lamellae with gradient channels. The lamellar thickness shown in Fig. 2(j) demonstrated an obvious decrease from the outermost layer to the inner center. BCNR contents had limited influence on the lamellar thickness, but they had obvious impacts on the gap distance of lamellar scaffolds. Fig. 2(k) shows that the gap distance increased from 40 to 100 µm upon addition of BCNRs. Moreover, higher amounts of BCNRs embedded in lamellae could increase the number of nuclei, which promoted SF self-assembly and water crystallization.

Secondary and crystal structure analyses

The crystal structures of the composite scaffolds were analyzed using SR-WAXD. Studies have shown that the mechanical properties of silk materials are greatly influenced by their crystal structures.[44] Fig. 3(a) shows the 1D SR-WAXD diffractograms of BCNR and SF/BCNR composite scaffolds. The diffraction peaks of BCNRs became evident when the BCNR content increased. Also, 2D SR-WAXD patterns revealed that the indices of the crystallographic plane of BCNR ([200]) was more distinct, indicating the existence of BCNRs. The crystalline-structure parameters of SF from SR-WAXD were calculated using Scherrer's formula and are listed in Table S1 (ESI†).[45,46]

Crystal morphology of silk is cubic and its volume can be approximated by $L_a \times L_b \times L_c$.[47] Results from the approximation (Table S1, ESI†) indicated that the crystal size and crystallinity of the SF increased upon addition of BCNRs. This might have been because the BCNRs were orientated to induce further crystallization
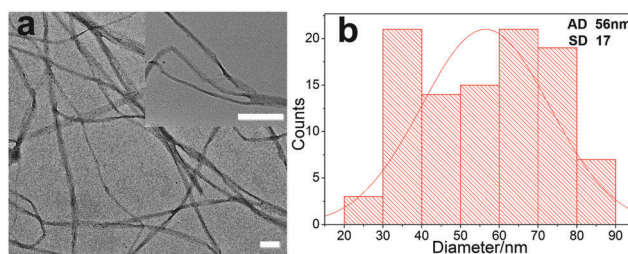

Fig. 1 (a) TEM image (an inset shows the bifurcate structure of BCNR) and (b) diameter distribution of BCNRs. Scale bars = 200 nm. The average diameter (AD) and standard deviation (SD) of BCNR were 56 and 12 nm, respectively.
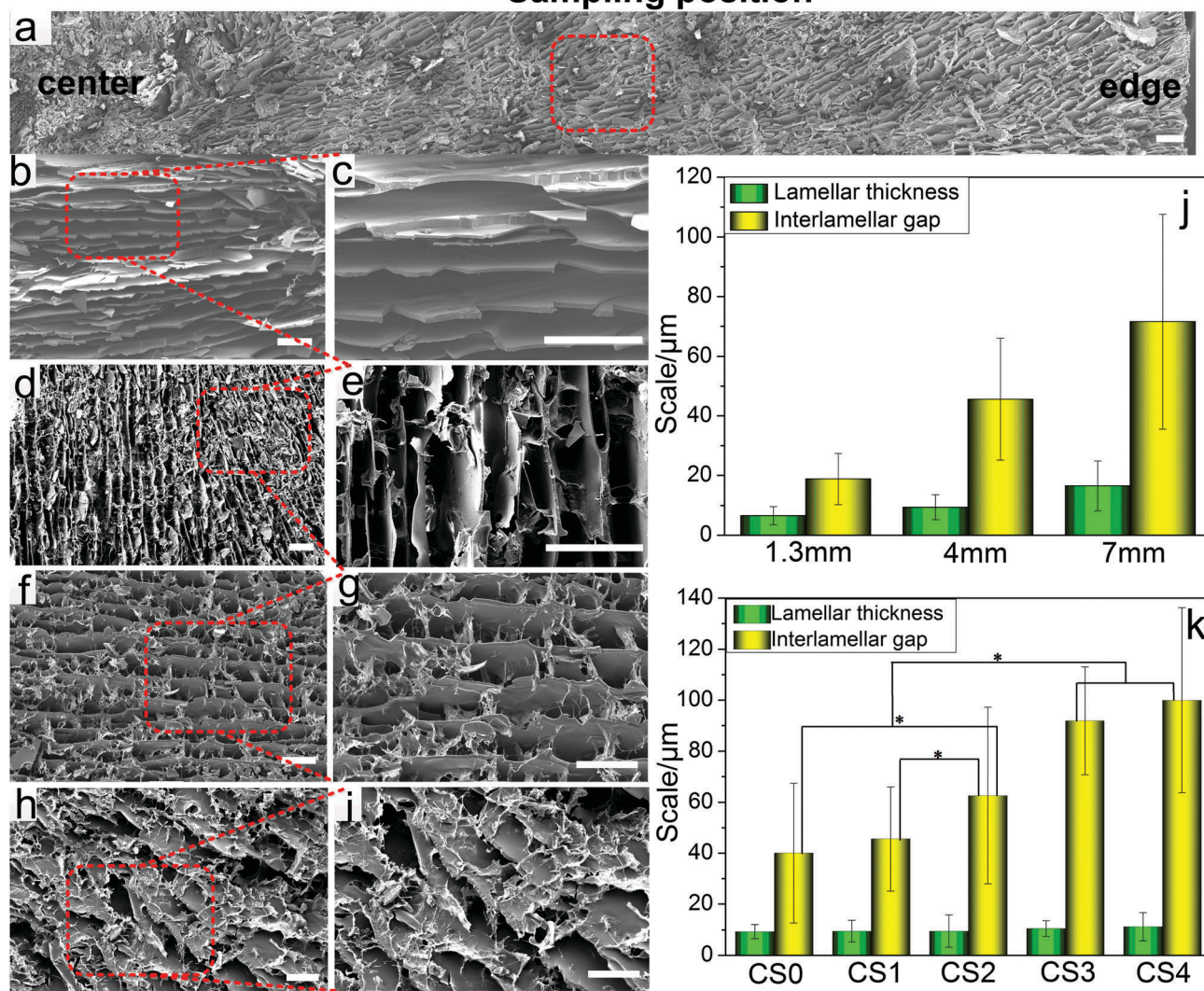
Sampling position

Fig. 2 Cross-sectional SEM images of: (a) CS1 along the radial direction, (b and c) CS0, (d and e) CS2, (f and g) CS3, and (h and i) CS4. To compare the gap distance and lamellae thickness, images from (b–i) were taken from an area 4 mm away from the center of the scaffold cylinder. Scale bar = 200 μm. Lamellar thickness and interlamellar gap distance of (j) CS1 composite scaffolds from the axis to the outer surface of the cylindrical scaffolds, and (k) composite scaffolds with different BCNR contents. All values in (k) were measured in an area 4 mm away from the center of the scaffold cylinder ($p < 0.05$).

of the SF molecule chains. The high content of BCNRs may start to entangle together and serve as a "crystal nucleus" for the formation of larger SF crystals during stirring. Unfortunately, the crystallinity of SF in composite scaffolds could not be calculated accurately due to the influence of strong crystal diffraction peaks. Given this situation, the effect of BCNRs on the secondary structure of SF in the composite scaffolds was investigated using FTIR spectroscopy.

As shown in Fig. 3(c), the peaks at 1032, 1058, and 1108 cm^{-1} were more distinct with increased BCNR contents. These peaks were the classical characteristic peaks of cellulose, which confirmed the presence of BCNRs.[48] The absorbance peaks at 1233 and 1650 cm^{-1} corresponded to the random coils/α-helix conformation of SF. The peaks at 1266, 1623, and 1697 cm^{-1} were assigned as β-sheets of SF, but the peak at 1678 cm^{-1} represented β-turn.[49] The wavenumbers between 3550 cm^{-1} and 3200 cm^{-1} were the results of the stretching of hydroxyl groups

from intermolecular and intramolecular hydrogen bonds.[50] The peak intensity (Fig. S1, ESI†) at 3286 cm^{-1} increased with increasing BCNR contents, indicating strong hydrogen-bonding interactions between BCNRs and SF.[51] Hence, it could be concluded that the addition of BCNRs into SF could augment additional hydrogen bonds, which eventually led to promotion of a more solid network structure of the BCNRs. Absorbance peaks from 1580 to 1720 cm^{-1} (amide-I region of SF) were not observed in BCNRs, so it was possible to calculate the conformation contents of SF from deconvolution plots so that the influence of BCNR peaks could be avoided. The deconvolution plots in the amide-I region of SF are shown in Fig. S2 (ESI†), and the corresponding deduced contents of β-sheet, β-turn, and random coil/α-helix are shown in Fig. 3(d). The SF in composite scaffolds of higher BNCRs had higher β-sheet but lower random coils/α-helix contents. This indicated that the BCNRs may induce the conformational
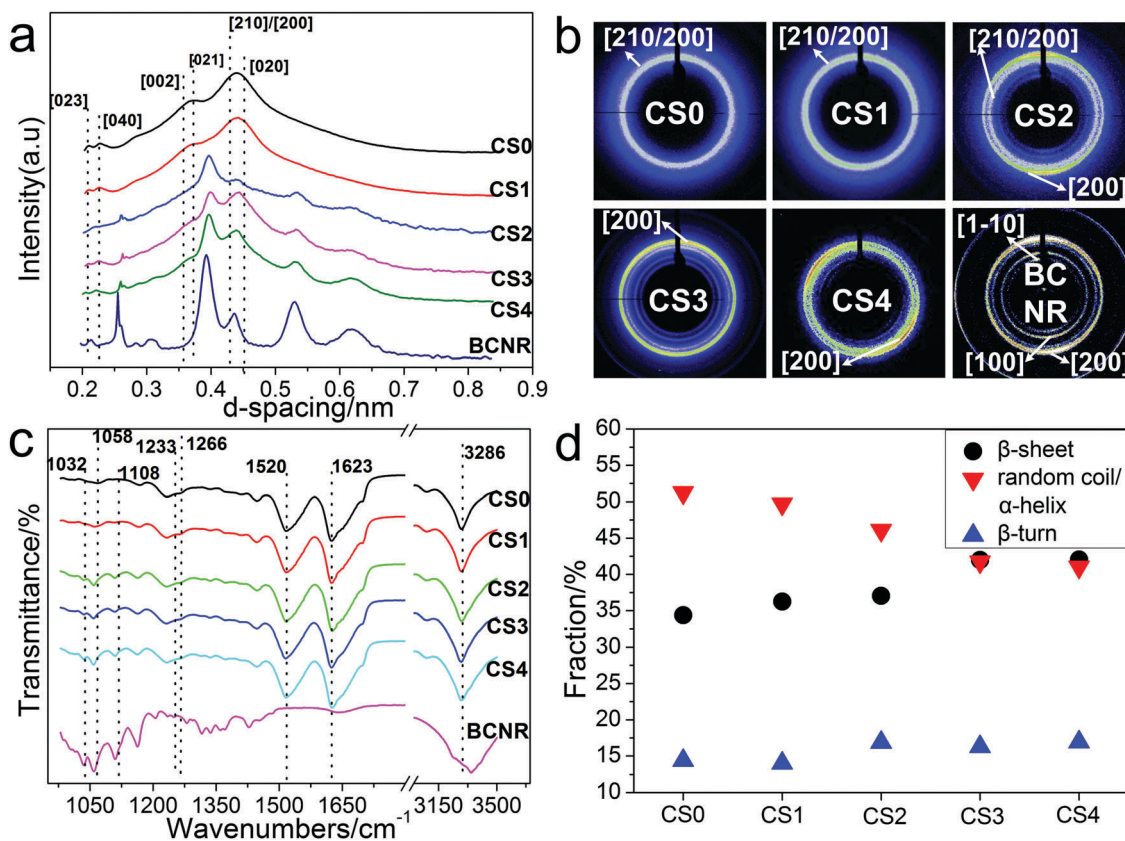
Fig. 3 (a) 1D SR-WAXD diffractograms of BCNR and SF/BCNF composite scaffolds of different BCNR contents and (b) its corresponding 2D SR-WAXD diffractograms. (c) FTIR spectra and (d) the deconvolution result of composite scaffolds in amide I of silk fibroin.

transition of SF from random coils/α-helix to well-organized β-sheets. This transformation might be beneficial to further improve mechanical properties of the scaffolds.

Mechanical properties

Fig. 4(a) shows the compressive strength–strain curves of different composite scaffolds. It can be seen that the compressive strength of CS0 was very low and fluctuated with strain, which indicated that it may be inappropriate for bone tissue engineering. All other scaffolds showed typical and consistent compressive strength–strain patterns. The scaffolds had an elastic deformation during initial strain, from which the compressive modulus was obtained. The strength then changed slightly with increasing strain, at which the gaps between lamellae were gradually compressed, leading to an increase in stress. Finally, when the scaffolds were compressed to 50% compressive strain (Fig. 4(d)), most of the lamella gaps collapsed and consequently caused a dramatic increase in the compressive strength (Fig. 4(a)). As shown in Fig. 4(b), the compressive strength of the composite scaffolds increased with increasing content of BCNRs until the mass ratio of BCNRs/SF reached 3 : 20, and started to decline when the ratio reached 4 : 20.

Porosity, swelling ratio, and water uptake

Porosity and water uptake are important factors in tissue engineering because they are used to compare the biomaterial properties of different scaffolds.[52] It can be seen from Fig. 5 that

the porosity of the scaffolds decreased slightly with increasing BCNRs content, and this could be attributed to the increase of bare BCNRs between the lamellae. Penetratable microchannels with high porosity can provide improved passages to guide cell migration, flow of nutrient solution and metabolic waste, and tissue ingrowth. Water uptake initially improved with an increase in BCNRs contents, which might have been due to high water-absorbing capacity of BCNRs.[33,53] When the mass ratio of BCNRs/SF was more than 2 : 20 (CS2), the high penetration density of the BCNRs may serve as "reinforcing pillars" in the intercalation structure, confining the further swelling of SF lamellae and BCNRs in the bounded space with relatively lower porosity, and subsequently causing water uptake to decrease. However, the scaffolds had high water-binding ability as a whole, which may have been attributed to the radial channel structure and BCNRs. The swelling ratio of the scaffolds increased initially with increasing contents of BCNRs up to a BCNRs/SF mass ratio of 2 : 20 but decreased when more BCNRs were added: this phenomenon could be explained by water uptake.

Cell morphology on scaffolds

The morphology of MC3T3 bone cells on scaffolds was observed by fluorescence microscopy and SEM after 5 days of culture. As shown in Fig. 6(a and b), small numbers of bone cells (which were small and spherical) were observed, which indicated that most of the cells did not adhere to the scaffolds at 1 day.

3644 | J. Mater. Chem. B, 2017, 5, 3640–3650

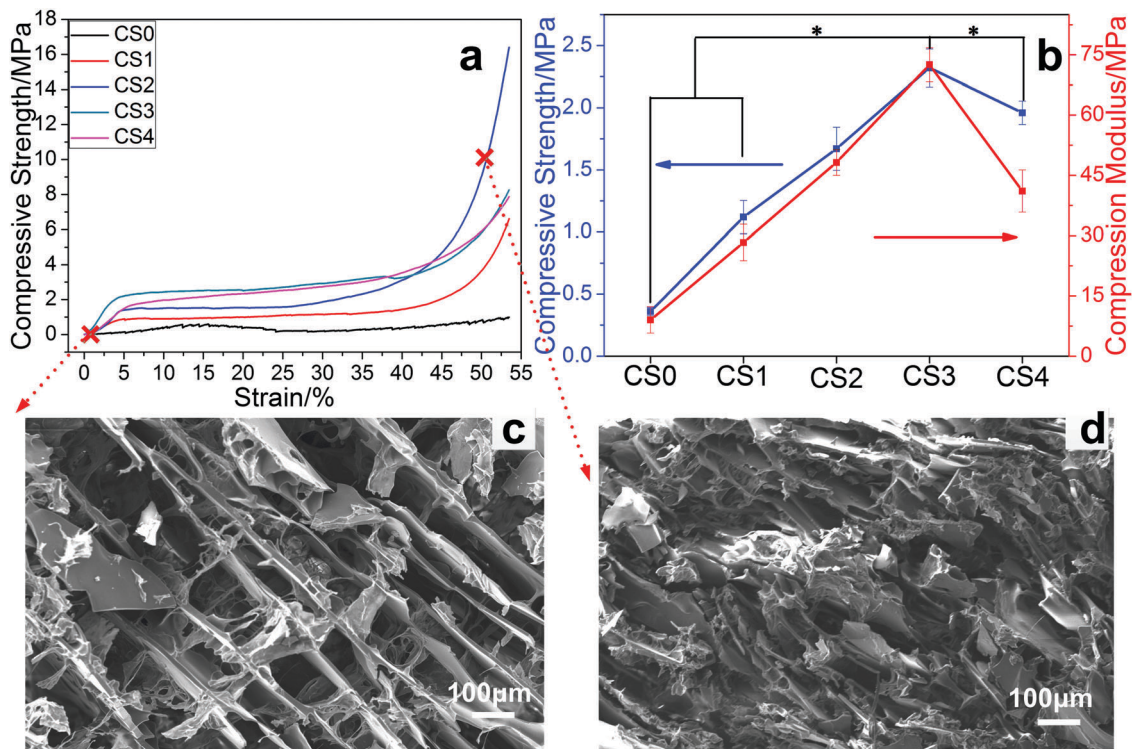This journal is © The Royal Society of Chemistry 2017

Fig. 4 (a) Compressive strength–strain curves and (b) compressive strength and modulus of SF/BCNR scaffolds of different BCNR contents ($p < 0.05$). SEM images of CS2: (c) before compression and (d) at 50% compressive strain.

This might have been because the inoculation procedures could lower the activity of bone cells. Fluorescence microscopy images from 2 days of culture (Fig. 6(c and d)) showed that the number of bone cells increased from day 1, which indicated that bone cells adhered to the surface of the scaffolds. Images from 3 and 5 days of culture (Fig. 6(e–h)) demonstrated that the bone cells were uniformly spread out and migrated around the scaffolds. The pseudopodium of bone cells adhered tightly to the lamellae surface (Fig. 6(i and j)), which showed the excellent biocompatibility of the composite scaffolds. According to the literature,[54,55] micropores in scaffolds boost the homogeneity of bone distribution through a capillary effect to improve bone regeneration. Therefore, our composite scaffolds with radial microchannels and an intercalation structure may also have had a similar capillary effect, and were beneficial for bone regeneration.

In vitro bone bioactivity assay

Bone bioactivity of composite scaffolds was conducted by soaking the scaffolds into SBF for 5 days. The SEM images shown in Fig. 7 demonstrate more depositions of apatite on the scaffolds upon addition of BCNRs. In contrast, in pure SF scaffolds (CS0), mineralized apatite spherules were deposited only on the lamellar surfaces. In the case of composite scaffolds (Fig. 7(b–e)) however, the mineralized apatite started to fill the gap, which indicated that the scaffolds with higher BCNR contents had improved mineralization. The mineralization ratio of CS0, CS1, CS2, CS3, and CS4 was 13.2%, 39.8%, 42.3%, 51.1%, and 71.3%, respectively. The higher BCNR contents on the scaffold lamellar surface

induced a more favorable nucleus for hydroxyapatite crystals to grow.[43,56] The mineralized composite scaffolds will have more favorable bone-repair ability due to improved osteoinductive activity and mechanical strength.[57]

As shown in Fig. 7(f), the optical density (OD) values of different composite scaffolds increased from day 1 to day 7. However, no significant differences in OD values were observed in all scaffolds from day 1 to day 3 due to the low density of cells. The OD values of CS2, CS3, and CS4 scaffolds were significantly higher than those of tissue culture plastics (TCPs) at day 5. The OD values of CS3 and CS4 were nearly 2.5-times higher compared with those of the control groups (coverslips) at day 7. These results indicated that the composite scaffolds had good biocompatibility for bone cells. Moreover, they demonstrated that an "interlamellar bridge", rough surface,[8,58] and augmentation of gap distance may favor the adhesion and proliferation of the bone cells.

Discussion

Balance between pore structure and mechanical properties

It is known that the pore structure and mechanical strength are important factors for bone repair scaffolds. With regard to mechanical properties, scaffolds should match the compressive strength and modulus of the implantation site or at least be able to allow cells to attach and proliferate sustainably. With respect to pore structure, the scaffolds should have a highly interconnected 3D pore structure for the growth and migration of bone cells, and for other mass transmissions.[59] However, a
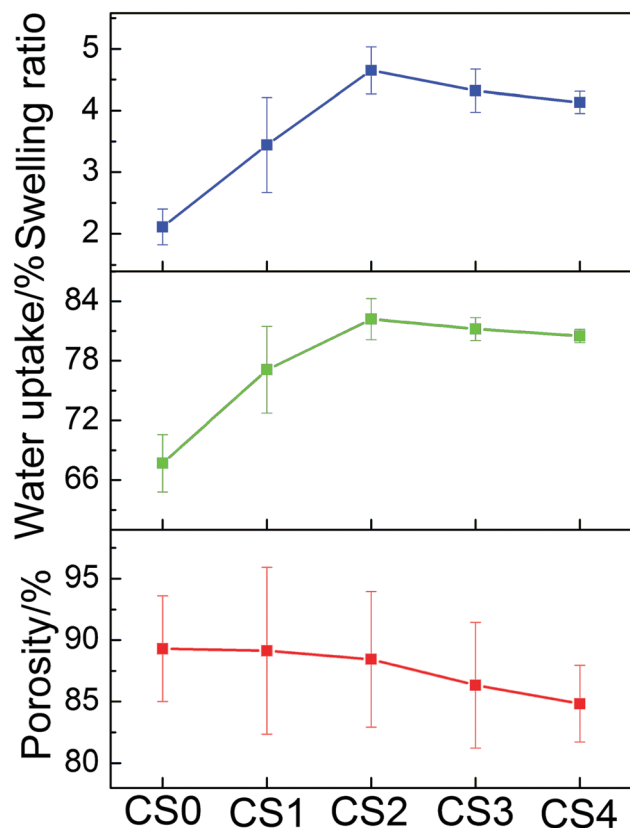
This journal is © The Royal Society of Chemistry 2017

J. Mater. Chem. B, 2017, 5, 3640–3650 | 3645

Fig. 5 Porosity, water-uptake ratio, and swelling ratio of SF/BCNR composite scaffolds of various BCNR contents.

Fig. 6 Fluorescence microscopic images of CS0 (a, c, e and g) and CS3 (b, d, f and h) scaffolds seeded with MC3T3 for 1 day (a and b), 2 days (c and d), 3 days (e and f), and 5 days (g and h). Cross-sectional (i) and longitudinal (j) SEM images of CS3 scaffolds seeded with bone cells for 3 days.

large and irregular pore size usually leads to poor mechanical properties. Thus, it is necessary to control the mechanical properties of the scaffolds by achieving appropriate pore structures.

Formation mechanism of radial lamellae and intercalation structure

When SF/BCNR suspension was initially placed at −25 °C, it started to exchange heat with its surrounding environment. The outermost layer of the suspension first met the ice-freezing point due to the high thermal conductivity of the metal mold. Thus, the water in the SF/BCNR mixture started to crystallize along the direction of the increasing temperature gradient that was formed from the outer shell to the axis of the mold. The first freezing temperature of −25 °C was much higher than the second freezing temperature of −80 °C, the ice had sufficient time to grow. SF became concentrated, which led to simultaneous aggregation and thus formation of lamellae; their shape was, however, restricted by the ice template. During the freeze-drying process, the ice crystals were evaporated and lamellar scaffolds were generated. Because the outermost layer of the mixture first reached the icing point, the ice crystals near the edge of the mold had longer time to grow, and consequently created laminar gaps with a larger distance formed after lyophilization (Fig. 2(a) and (j)). Similarly, the SF molecules near the edge of the mold had more time for self-assembly or aggregation than the SF molecules near the axis of the mold. Therefore, the lamellae thickness gradually
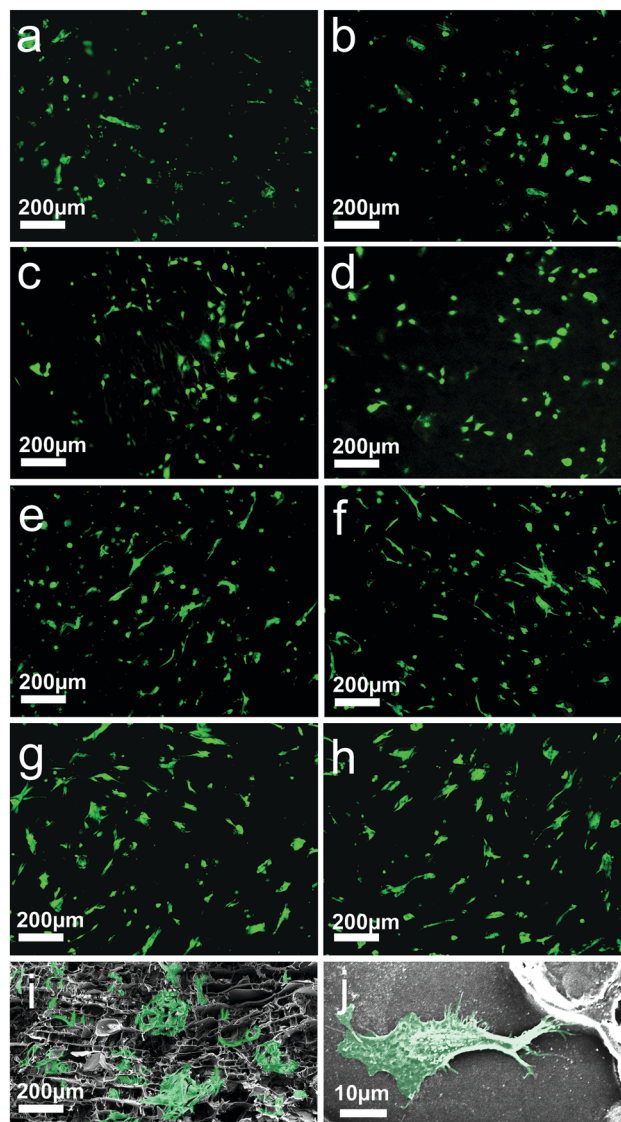
increased outwards. The SF/BCNRs mixture was a suspension with minor dispersed BCNRs in major SF solution, so a BCNRs matrix with low mobility might retain its original network and some nanoribbons aggregate to microfibers during freeze-drying. Consequently, an intercalation structure with SF lamellae- and BCNR-reinforcing networks was formed (Fig. 8).

The pore morphology of the scaffolds prepared by lyophilization can be controlled by adjusting the concentration of the solute, freezing temperature, freezing rate,[60] and pH.[61] Oliveira studied the effect of SF concentration, freezing temperature, and different post-treatments on the morphology of scaffolds.[25] Zhang *et al.* prepared SF scaffolds with uniaxial channels by directional freezing using liquid nitrogen.[62] Most scaffolds prepared by lyophilization utilize ice formation to control pore size.[25,62–64] Little attention has been paid to the effects of nanofillers and

3646 | *J. Mater. Chem. B*, 2017, **5**, 3640–3650
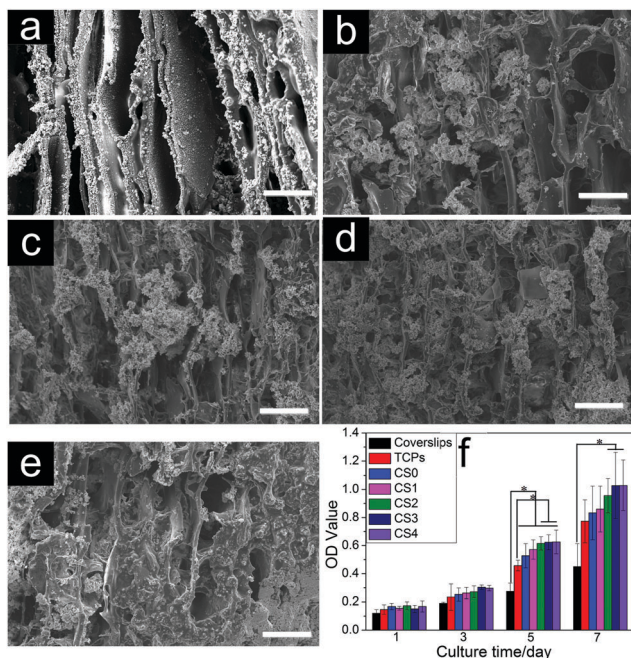
This journal is © The Royal Society of Chemistry 2017

Fig. 7 SEM image of different SF/BCNR composite scaffolds immersed in SBF for 5 days: (a) CS0, (b) CS1, (c) CS2, (d) CS3, and (e) CS4. Scale bar: 50 μm. (f) OD values of MC3T3 cells cultured on SF/BCNR composite scaffolds with different BCNR contents ($p < 0.05$, $n = 3$).

mechanical disturbance on the size and structure of pores. In this work, a new approach to control the pore size or interlamellar gap without changing the concentration of solute or freezing parameters was presented. Interlamellar gap distances ranging from 40 to 100 μm could be controlled by changing the content of BCNRs.

Reinforcement of the porous scaffolds

Scaffolds with high compressive strength and modulus have significant effects on bone tissue engineering not only to provide support for the adhesion and multiplication of cells, but also to promote osteogenic differentiation. Mechanical properties of SF scaffolds could be improved by self-reinforcement and external strengthening. Self-reinforcement mainly includes methanol treatment, water annealing, and steam sterilization. Oliveira *et al.* investigated three reinforcement methods for SF scaffolds.[25] In steam sterilization treatment, the highest compressive strength and modulus achieved were 22.5 and 290 kPa, respectively. External strengthening mainly includes fiber or nanofiller reinforcement and mineralization. Mobini *et al.* fabricated a silk-based composite scaffold strengthened by degummed silk fibers.[65] They achieved the highest compressive strength and modulus of 1.5 and 17.95 MPa (dry state), respectively. Mandal *et al.* reported a SF-based composite scaffold reinforced by micron-sized silk fibers (10–600 μm) obtained by utilizing alkali hydrolysis.[8] They improved the compressive modulus to ≈13 MPa in a hydrated state. Similarly, Bai *et al.* prepared tunable mechanical SF scaffolds with added SF nanofiber obtained by incubating SF solution at 60 °C.[26] The compressive modulus was tuned from 5 to 16.7 kPa (hydrated state). Zheng *et al.* prepared oxidized SF solution by chemical oxidation utilizing NaClO
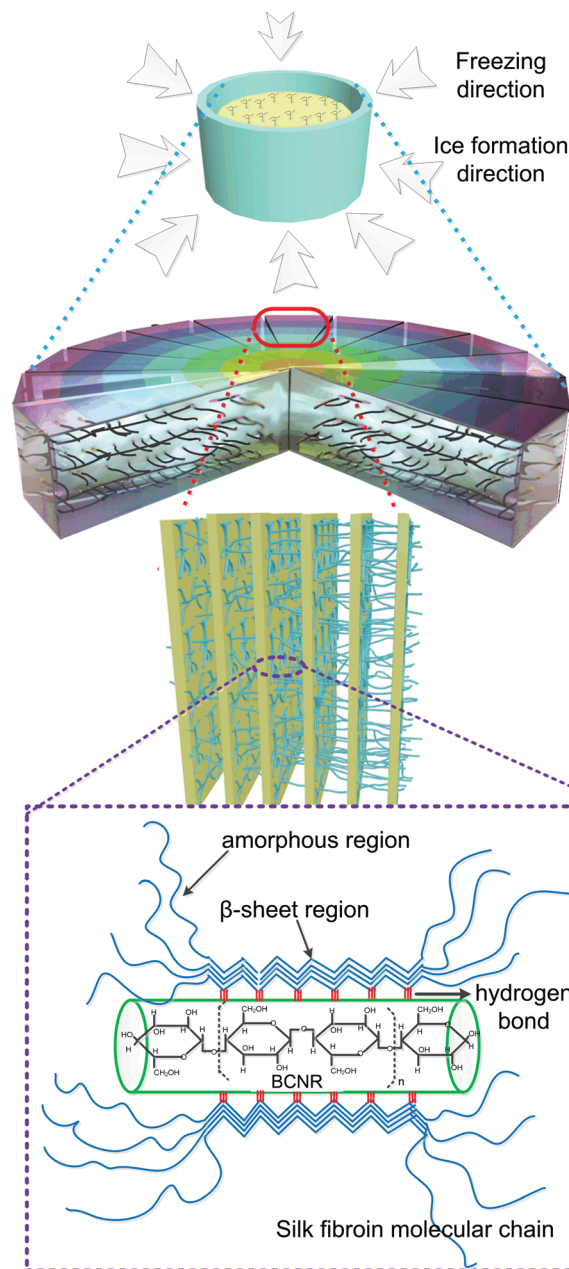

Fig. 8 Formation mechanism of radial lamellae and intercalation structure.

to bring more carboxyl groups in SF.[66] The achieved compressive modulus of the untreated, oxidized, and mineralized SF scaffolds was 18 ± 6, 211 ± 75, and 758 ± 189 kPa (hydrated state), respectively. Although these attempts improved the compressive strength and modulus of porous SF scaffolds, they were much weaker than scaffolds presented in this work. Here, we combined BCNR fillers and ethanol treatment to reinforce SF scaffolds, and achieved compressive strength and compressive modulus of 2.32 and 72.5 MPa, respectively (sample CS3), which reached the range of cancellous bone.

From a micro-scale viewpoint, strong molecular interactions between BCNRs and SF were observed in FTIR spectra. BCNRs promoted the transition of the SF conformation from random

coils/α-helix to well-organized β-sheets (Fig. 8). Ethanol treatment also contributed to β-sheet formation, which contributed (at least in part) to the mechanical strength of the scaffolds. From a macro-scale viewpoint, because the BCNRs have a wide-length distribution, nanoscale diameter, and fibrillar structure, parts of BCNRs may embed between the lamellae whereas others penetrate vertically into the lamellae as reinforcing pillars. This intercalated structure prevented slipping of lamellae while dispersing stress to avoid stress concentration that could destroy the scaffold structure (Fig. 8). Excessive amounts of BCNRs, however, might lead to uneven distributions to generate flaws in the scaffolds and, as a result, the mechanical properties of the CS4 scaffolds deteriorate. Scaffold CS3 had the highest strength and modulus of 2.32 and 72.5 MPa, respectively. These properties are in the range of cancellous bone (compressive strength = 2–12 MPa; compressive modulus = 0.05–5 GPa).[67] Considering the pore structure, although the gap distance increased with increasing BCNRs content, lamellar structure was clear and obvious only for CS0 to CS3. When the mass ratio of BCNRs/SF contents reached 4 : 20 (CS4), excessive amounts of BCNRs were incorporated between the gaps. It is not possible to observe the complete lamellar structure because some lamellae may be broken and/or restricted by BCNRs. Upon addition of BCNRs, the surface of lamellae became rougher so that more BCNRs could penetrate between lamellae. Chang et al. developed various porous hydroxyapatite scaffolds with pore configurations to assess osteo-conduction.[68] They found that a 50 μm pore size was large enough for osteoconduction. Thus, CS1 to CS4 scaffolds have effective pore size (determined by interlamellar gap distance) for osteo-conduction. CS3, however, was the best candidate for composite scaffold owing to its large and balanced interlamellar gap distance, and excellent mechanical properties.

Degradation analyses

According to a preliminary calculation from Fig. 3, the difference in crystallinity among the SF/BCNR composite scaffolds was not significant (≈50%). In work by Kim et al.,[20] the in vitro degradation of 3D SF porous scaffolds with similar crystallinity (≈48%) was evaluated. The mass of scaffold derived from 8% silk solution decreased to 30% after 21 days in the presence of a protease due to degradation. In addition, after implantation in Lewis rats for 8 weeks, the signs of degradation became visible and most scaffolds derived from 6% or 10% silk solution were completely degraded at the end of 1 year.[69] The rate of degradation decreased when the concentration of SF solution increased in vitro and in vivo. This finding demonstrates that degradation of the scaffold was tunable. It can be predicted that the SF in composite scaffolds presented in this work may have similar degradation behavior as the scaffolds in the literature due to their similar crystallinity.

With regard to the bacterial cellulose nanoribbon, it cannot be biodegraded in the human body due to a lack of chemical or enzymatic processes that can hydrolyze the beta-1,4-glucose linkages of the cellulose.[70,71] However, this material can be degraded by incorporating the enzyme cellulose.[71–73] Also, by changing the cellulose content, the degradation rate could be controlled to match the growth rate of different tissues.

Benefit of a gradient structure scaffold for bone tissue regeneration

Scaffolds with a gradient structure are not only a good transition between bone and cartilage tissue for biomimetic structures, but they are also perfect devices because they can transport nutriments and waste by capillary action.[74] Bai et al. developed a modified ice-templating method to fabricate a ceramic gradient scaffold which had cell self-seeding ability by a capillary effect while in contact with a cell solution.[55] In recent years, considerable research has been conducted to fabricate various gradient scaffolds, including a gradient geometry structure,[75,76] gradient growth factor concentrations,[77] and biocomposition,[78] to improve bone repair. This "intelligent" scaffold could promote more regular cell inoculation and improve bone regeneration while reducing the requirement for complicated clinical procedures.

Conclusion

Three-dimensional SF/BCNR composite scaffolds with radial lamellar patterns and gradient lamellar gap distance were achieved using a multi-staged freeze-drying method with temperature gradients. Addition of BCNRs to SF increased the lamellar thickness, enlarged the gap distance, and greatly reinforced scaffolds with an intercalation structure. The embedded BCNRs enhanced the lamellar strength, and the penetrated fibers could help avoid slippage of the lamellae while dispersing stress. Moreover, the intercalated BCNRs network improved water uptake and the swelling ratio of the composite scaffolds. The interconnected porous structure facilitated flow of nutrients or waste to maintain cell viability. The robust mechanical performance, improved cell adhesion, and bone-bonding ability of the biodegradable SF/BCNRs scaffolds provides potential for further bone regeneration applications.

Acknowledgements

Notes and references

1 D. Logeart-Avramoglou, F. Anagnostou, R. Bizios and H. Petite, J. Cell. Mol. Med., 2005, 9, 72.
2 T. Kokubo, H. M. Kim and M. Kawashita, Biomaterials, 2003, 24, 2161–2175.

3 L. Uebersax, T. Apfel, K. M. Nuss, R. Vogt, H. Y. Kim, L. Meinel, D. L. Kaplan, J. A. Auer, H. P. Merkle and R. B. Von, *Eur. J. Pharm. Biopharm.*, 2013, **85**, 107.

4 I. Kovach, J. Rumschöttel, S. E. Friberg and J. Koetz, *Colloids Surf., B*, 2016, **145**, 347–352.

5 R. Hernández-Córdova, D. A. Mathew, R. Balint, H. J. Carrillo-Escalante, J. M. Cervantes-Uc, L. A. Hidalgo-Bastida and F. Hernández-Sánchez, *J. Biomed. Mater. Res., Part A*, 2016, **104**, 1912–1921.

6 Z. Zhao, J. Wang, J. Lu, Y. Yu, F. Fu, H. Wang, Y. Liu, Y. Zhao and Z. Gu, *Nanoscale*, 2016, **8**, 13574–13580.

7 K. F. Leong, C. M. Cheah and C. K. Chua, *Biomaterials*, 2003, **24**, 2363–2378.

8 B. B. Mandal, A. Grinberg, E. S. Gil, B. Panilaitis and D. L. Kaplan, *Proc. Natl. Acad. Sci. U. S. A.*, 2012, **109**, 7699–7704.

9 A. Hamlekhan, M. Mozafari, N. Nezafati, M. Azami and A. Samadikuchaksaraei, *Key Eng. Mater.*, 2012, **493–494**, 909–915.

10 M. Bühler, P. E. Bourban and J. A. E. Månson, *Compos. Sci. Technol.*, 2008, **68**, 820–828.

11 V. R. King, M. Henseler, R. A. Brown and J. V. Priestley, *Exp. Neurol.*, 2003, **182**, 383–398.

12 Z. Li, Q. Liu, H. Wang, L. Song, H. Shao, M. Xie, Y. Xu and Y. Zhang, *ACS Biomater. Sci. Eng.*, 2015, **1**, 238–246.

13 Q. Liu, J. Huang, H. Shao, L. Song and Y. Zhang, *RSC Adv.*, 2016, **6**, 7683–7691.

14 Y. Wu, Z. Wang, J. Y. Fuh, Y. S. Wong, W. Wang and E. S. Thian, *J. Mater. Sci.: Mater. Med.*, 2016, **27**, 115.

15 M. H. Zaman, L. M. Trapani, A. L. Sieminski, D. Mackellar, H. Gong, R. D. Kamm, A. Wells, D. A. Lauffenburger and P. Matsudaira, *Proc. Natl. Acad. Sci. U. S. A.*, 2006, **103**, 10889–10894.

16 D. Dado and S. Levenberg, *Semin. Cell Dev. Biol.*, 2009, **20**, 656.

17 S. Evenram, V. Artym and K. M. Yamada, *Cell*, 2006, **126**, 645–647.

18 P. Rider, Y. Zhang, C. Tse, Y. Zhang, D. Jayawardane, J. Stringer, J. Callaghan, I. M. Brook, C. A. Miller and X. Zhao, *J. Mater. Sci.*, 2016, **51**, 8625–8630.

19 R. F. P. Pereira, M. M. Silva and D. Z. B. Verónica, *Macromol. Mater. Eng.*, 2015, **300**, 1171–1198.

20 U. J. Kim, J. Park, H. J. Kim, M. Wada and D. L. Kaplan, *Biomaterials*, 2005, **26**, 2775–2785.

21 G. M. Nogueira, R. F. Weska, W. C. Vieira Jr, B. Polakiewicz, A. C. D. Rodas, O. Z. Higa and M. M. Beppu, *J. Appl. Polym. Sci.*, 2009, **114**, 617–623.

22 R. R. Jose, J. E. Brown, K. E. Polido, F. G. Omenetto and D. L. Kaplan, *ACS Biomater. Sci. Eng.*, 2015, **1**, 780–788.

23 R. Nazarov, H. J. Jin and D. L. Kaplan, *Biomacromolecules*, 2004, **5**, 718.

24 M. O. Montjovent, L. Mathieu, B. Hinz, L. L. Applegate, P. E. Bourban, P. Y. Zambelli, J. A. Månson and D. P. Pioletti, *Tissue Eng.*, 2005, **11**, 1640–1649.

25 A. L. Oliveira, L. Sun, H. J. Kim, X. Hu, W. Rice, J. Kluge, R. L. Reis and D. L. Kaplan, *Acta Biomater.*, 2012, **8**, 1530.

26 S. Bai, H. Han, X. Huang, W. Xu, D. L. Kaplan, H. Zhu and Q. Lu, *Acta Biomater.*, 2015, **20**, 22–31.

27 D. K. Kim, J. I. Kim, T. I. Hwang, B. R. Sim and G. Khang, *ACS Appl. Mater. Interfaces*, 2017, **9**, 1384–1394.

28 F. A. Sheikh, H. W. Ju, J. M. Lee, B. M. Moon, H. J. Park, O. J. Lee, J. Kim, D. Kim and C. H. Park, *Nanomedicine*, 2015, **11**, 681–691.

29 O. J. Lee, H. W. Ju, J. H. Kim, J. M. Lee, C. S. Ki, J. H. Kim, B. M. Moon, H. J. Park, F. A. Sheikh and C. H. Park, *J. Biomed. Nanotechnol.*, 2014, **10**, 1294–1303.

30 P. Bhattacharjee, D. Naskar, T. K. Maiti, D. Bhattacharya, P. Das, S. K. Nandi and S. C. Kundu, *Colloids Surf., B*, 2016, **143**, 431–439.

31 P. Bhattacharjee, B. Kundu, D. Naskar, H. W. Kim, D. Bhattacharya, T. K. Maiti and S. C. Kundu, *Cell Tissue Res.*, 2016, **363**, 525–540.

32 N. Yin, M. D. Stilwell, T. M. Santos, H. Wang and D. B. Weibel, *Acta Biomater.*, 2014, **12**, 129–138.

33 M. Ul-Islam, T. Khan and J. K. Park, *Carbohydr. Polym.*, 2012, **88**, 596–603.

34 H. X. Li, S. J. Kim, Y. W. Lee, D. K. Chang and I. K. Oh, *Korean J. Chem. Eng.*, 2011, **28**, 2306–2311.

35 H. G. Oliveira Barud, H. D. Barud, M. Cavicchioli, T. S. do Amaral, O. B. de Oliveira, D. M. Santos, A. L. D. A. Petersen, F. Celes, V. M. Borges, C. I. de Oliveira, P. F. de Oliveira, R. A. Furtado, D. C. Tavares and S. J. L. Ribeiro, *Carbohydr. Polym.*, 2015, **128**, 41–51.

36 H. Bäckdahl, G. Helenius, A. Bodin, U. Nannmark, B. R. Johansson, B. Risberg and P. Gatenholm, *Biomaterials*, 2006, **27**, 2141–2149.

37 X. Chen, F. Yuan, H. Zhang, H. Yang, J. Yang and D. Sun, *J. Mater. Sci.*, 2016, **51**, 5573–5588.

38 H. Bäckdahl, M. Esguerra, D. Delbro, B. Risberg and P. Gatenholm, *J. Tissue Eng. Regener. Med.*, 2008, **2**, 320–330.

39 H. Pan, Y. Zhang, H. Shao, X. Hu, X. Li, F. Tian and J. Wang, *J. Mater. Chem. B*, 2014, **2**, 1408–1414.

40 Y. Wang, E. Bella, C. S. D. Lee, C. Migliaresi, L. Pelcastre, Z. Schwartz, B. D. Boyan and A. Motta, *Biomaterials*, 2010, **31**, 4672–4681.

41 X. Zhang, C. Cao, X. Ma and Y. Li, *J. Mater. Sci.: Mater. Med.*, 2012, **23**, 315–324.

42 K. J. Woollard, S. Sturgeon, J. P. Chin-Dusting, H. H. Salem and S. P. Jackson, *J. Biol. Chem.*, 2009, **284**, 13110–13118.

43 T. Kokubo and H. Takadama, *Biomaterials*, 2006, **27**, 2907–2915.

44 K. Yazawa, K. Ishida, H. Masunaga, T. Hikima and K. Numata, *Biomacromolecules*, 2016, **17**, 1057–1066.

45 S. Sampath, T. Isdebski, J. E. Jenkins, J. V. Ayon, R. W. Henning, J. P. Orgel, O. Antipoa and J. L. Yarger, *Soft Matter*, 2012, **8**, 6713–6722.

46 Z. Chao, Y. Zhang, H. Shao and X. Hu, *ACS Appl. Mater. Interfaces*, 2016, **68**, 423.

47 R. E. Marsh, R. B. Corey and L. Pauling, *Biochim. Biophys. Acta*, 1955, **16**, 1.

48 L. Liu, X. Yang, H. Yu, C. Ma and J. Yao, *RSC Adv.*, 2014, **4**, 14304.

49 Q. Peng, Y. Zhang, L. Lu, H. Shao, K. Qin, X. Hu and X. Xia, *Sci. Rep.*, 2016, **6**, 36473.

This journal is © The Royal Society of Chemistry 2017

J. Mater. Chem. B, 2017, **5**, 3640–3650 | 3649

50 M. S. Peresin, Y. Habibi, J. O. Zoppe, J. J. Pawlak and O. J. Rojas, *Biomacromolecules*, 2010, **11**, 674–681.

51 D. J. Park, Y. Choi, S. Heo, S. Y. Cho and H. J. Jin, *J. Nanosci. Nanotechnol.*, 2012, **12**, 6139.

52 S. J. Hollister, *Nat. Mater.*, 2006, **4**, 518.

53 Z. Li, L. Wang, S. Chen, C. Feng, S. Chen, N. Yin, J. Yang, H. Wang and Y. Xu, *Cellulose*, 2015, **22**, 373–383.

54 L. E. Rustom, T. Boudou, S. Y. Lou, I. Pignot-Paintrand, B. W. Nemke, Y. Lu, M. D. Markel, C. Picart and A. W. Johnson, *Acta Biomater.*, 2016, **44**, 144–154.

55 H. Bai, D. Wang, B. Delattre, W. Gao, C. J. De, S. Li and A. P. Tomsia, *Acta Biomater.*, 2015, **20**, 113–119.

56 J. Dai, J. Bai, J. Jin, S. Yang and G. Li, *Adv. Eng. Mater.*, 2015, **17**, 1691–1697.

57 L. A. Cyster, D. M. Grant, S. M. Howdle, F. R. A. J. Rose, D. J. Irvine, D. Freeman, C. A. Scotchford and K. M. Shakesheff, *Biomaterials*, 2005, **26**, 697–702.

58 J. E. Davies, *Anat. Rec.*, 1996, **245**, 426–445.

59 D. W. Hutmacher, *Biomaterials*, 2000, **21**, 2529–2543.

60 F. J. O'Brien, B. A. Harley, I. V. Yannas and L. Gibson, *Biomaterials*, 2004, **25**, 1077–1086.

61 Q. Lu, Q. Feng, K. Hu and F. Cui, *J. Mater. Sci.: Mater. Med.*, 2008, **19**, 629–634.

62 Q. Zhang, Y. Zhao, S. Yan, Y. Yang, H. Zhao, M. Li, S. Lu and D. L. Kaplan, *Acta Biomater.*, 2012, **8**, 2628–2638.

63 S. Deville and A. P. Tomsia, *Science*, 2006, **311**, 515–518.

64 H. Zhang, I. Hussain, M. Brust, M. F. Butler, S. P. Rannard and A. I. Cooper, *Nat. Mater.*, 2005, **4**, 787.

65 S. Mobini, B. Hoyer, M. Solati-Hashjin, A. Lode, N. Nosoudi, A. Samadikuchaksaraei and M. Gelinsky, *J. Biomed. Mater. Res., Part A*, 2013, **101A**, 2392–2404.

66 Z. Ke, C. Ying, W. Huang, Y. Lin, D. L. Kaplan and Y. Fan, *ACS Appl. Mater. Interfaces*, 2016, 14406–14413.

67 Z. Esen, E. Bütev and M. S. Karakaş, *J. Mech. Behav. Biomed. Mater.*, 2016, **63**, 273–286.

68 B. S. Chang, C. K. Lee, K. S. Hong, H. J. Youn, H. S. Ryu, S. S. Chung and K. W. Park, *Biomaterials*, 2000, **21**, 1291–1298.

69 Y. Wang, D. D. Rudym, A. Walsh, L. Abrahamsen, H. J. Kim, H. S. Kim, C. Kirkerhead and D. L. Kaplan, *Biomaterials*, 2008, **29**, 3415–3428.

70 J. Wang, Y. Zhu and J. Du, *J. Mech. Med. Biol.*, 2011, **11**, 285–306.

71 B. Wang, X. Lv, S. Chen, Z. Li, X. Sun, C. Feng, H. Wang and Y. Xu, *Cellulose*, 2016, **23**, 1–12.

72 Y. Hu and J. M. Catchmark, *J. Biomed. Mater. Res., Part B*, 2011, **97**, 114–123.

73 Y. Hu and J. M. Catchmark, *Acta Biomater.*, 2011, **7**, 2835–2845.

74 L. A. Di, V. B. Clemens and M. Lorenzo, *Birth Defects Res., Part C*, 2015, **105**, 34–52.

75 T. B. Woodfield, J. Malda, W. J. De, F. Péters, J. Riesle and C. A. van Blitterswijk, *Biomaterials*, 2004, **25**, 4149–4161.

76 T. J. Levingstone, A. Matsiko, G. R. Dickson, F. J. O'Brien and J. P. Gleeson, *Acta Biomater.*, 2014, **10**, 1996–2004.

77 M. Singh, C. Berkland and M. S. Detamore, *Tissue Eng., Part B*, 2008, **14**, 341–366.

78 K. E. M. Benders, P. R. V. Weeren, S. F. Badylak, D. B. F. Saris, W. J. A. Dhert and J. Malda, *Trends Biotechnol.*, 2013, **31**, 169–176.